Computational Geosciences (2024) 28:77–90
https://doi.org/10.1007/s10596-023-10263-w

ORIGINAL PAPER

Parameterizing the fluid forces on limpet shells in unidirectional flow

Carley Walker[1,2] · Julian Simeonov[1] · Ian Adams[1,3]

Received: 16 September 2022 / Accepted: 6 November 2023 / Published online: 25 November 2023

Abstract
Current parameterizations of the hydrodynamic forces on irregular particles consider some shape dependencies, but lack an explicit dependence on the orientation with respect to the flow. In this paper, we propose a new parameterization of the drag and lift forces acting on whole Limpet shells at arbitrary orientations with respect to the direction of flow through the linear regression of fluid forces against the velocity components in an object frame of reference. The fluid forces were estimated using boundary layer-resolving Reynolds-averaged Navier-Stokes (RANS) simulations. We verified the accuracy of the shear stress transport (SST) $k-\omega$ turbulence model on flat plates with varying angles of attack, and we achieved coefficients of determination versus existing data of approximately 0.95 for both the drag and lift coefficients. From the linear regression of our simulated force data, we developed a model as a function of 3-dimensional orientations to predict the hydrodynamic forces acting on a Limpet shell with coefficients of determination of 0.80 for normal forces and 0.51 for longitudinal forces.

Keywords Limpet shell · Hydrodynamic forces · CFD modeling

1 Introduction

The distribution of shelly sediments on the shelf affects the hydrodynamic and acoustic properties of the seafloor and the habitat of bottom animals. One approach to understand the transport and distribution of sediments by the action of waves and currents is by means of Euler-Lagrange simulations that track the motion of individual particles. The Euler-Lagrange models for sediment transport require parameterizations of the drag and lift force coefficients acting on these particles. Current parameterizations of force coefficients for irregular particles have considered mainly the effect of shape but not the 3-dimensional orientation of the particles [16, 17].

✉ Julian Simeonov
julian.simeonov@nrlssc.navy.mil

Carley Walker
walker.carley@yahoo.com

Ian Adams
ian.adams.ctr@nrlssc.navy.mil

1 Ocean Sciences Division, US Naval Research Laboratory, Stennis Space Center, MS 39529, USA

2 Leidos Innovation Center, Leidos, San Diego, CA, USA

3 National Research Council Research Associateship Program, Washington, DC 20001, USA

The goal of this paper is to develop an effective and robust parameterization of the drag and lift coefficients for forces on a whole Limpet shell that has an arbitrary orientation to the flow direction. The hydrodynamic forces acting on Limpet shells in a unidirectional flow have been studied in a number of laboratory experiments [10, 11]. However, these experiments considered only three convex side-up orientations such that the shell was oriented with the anterior, posterior, and lateral side of the shell facing the inlet of flow.

It is well known that hydrodynamic forces on airfoils can have complicated non-linear dependence on the orientation (see for example Figs. 3 and 4 of Ahmad 2005 [9]). The consideration of the angle of attack of mainstream flow on objects has been discussed in various other works such as from Jones et al. 2002, Ortiz et al. 2015, and Sun et al. 2018 [5, 7, 14]. In previous work, Jones et al. considered functions of angle of attack for solving the hydrodynamic forces acting on submerged torpedoes in simulation. They defined the longitudinal and lateral hydrodynamic forces, X and Z, respectively, as

$$X = \frac{1}{2}\rho V^2 A_{ref}\left(c_l \sin\alpha - c_d \cos\alpha\right) \tag{1}$$

and

$$Z = -\frac{1}{2}\rho V^2 A_{ref}\Big(c_l \cos\alpha + c_d \sin\alpha\Big), \tag{2}$$

where c_l and c_d are the lift and drag coefficients, respectively, α is angle of attack, ρ is the density of the water, A_{ref} is a reference area, and V is the velocity magnitude. Our goal is to extend such explicit models for the drag and lift coefficients to three dimensions [14]. In another work, Ortiz et al. used wind tunnel experiments to consider the aerodynamic loads on flat plates with varying aspect ratios and angles of attack, and they noticed that the ratio of the aerodynamic drag and lift coefficients, c_d and c_l, in an object frame of reference closely followed the following equation introduced by Torres et al. 2004 [7, 15]:

$$c_d/c_l = \tan\alpha, \tag{3}$$

where α is angle of attack. We will compare this ratio with the ratio obtained from the force parameterizations considered in this manuscript.

Considering different shapes such as ellipsoids and fibres, Sun et al. analyzed the drag coefficients of graphite dust in a high temperature gas cooled reactor (HTGR) using a computational fluid dynamics model [5]. Using a drag coefficient framework introduced by Rosendahl 2000, Sun et al. considered the following formula for the drag coefficients [1]:

$$c_d(\alpha) = c_{d,\alpha=0^\circ} + (c_{d,\alpha=90^\circ} - c_{d,\alpha=0^\circ})\sin^{\mu_0}\alpha \tag{4}$$

where α is the angle of incidence and the orientation, μ_0 is a coefficient estimated based on the shape of the particle using numerical data and the least squares method, and $c_{d,\alpha=0^\circ}$ and $c_{d,\alpha=90^\circ}$ are coefficients depending on the shape and the Reynolds number. We will examine this dependence in relation to our parameterization of the fluid forces in an object frame of reference.

Here, we propose a new parameterization of forces for arbitrary orientations, which assumes that the force vector in the object frame of reference is related to the flow vector in the object frame of reference by nine unique tensor coefficients which are independent of the orientation. To test this parameterization, we first carried out Reynolds-Averaged Navier-Stokes (RANS) simulations for flow around a rectangular plate and whole Limpet shells in order to estimate the drag and lift forces at different orientations. The new parameterization and RANS methodology are described in the Methods section. In the Validation section, we validated the RANS simulations by comparing the drag and lift forces with the laboratory experiments of Denny 1989 for Limpet shells and Ortiz et al. 2015 for the rectangular plate, respectively. In the Discussion section, we used a linear regression between the force and velocity components in the object frame of reference to determine the nine force coefficients and evaluated the performance of the new force parameterization against the simulated forces [7, 10].

2 Methods

2.1 A parameterization of the fluid forces

Our goal is to develop a predictive model for hydrodynamic forces acting on an irregular particle with an arbitrary orientation with respect to the flow direction. The hydrodynamic force is often defined as

$$F_j = \frac{1}{2}u_1 \rho C_j A_j ||u||, \tag{5}$$

where ρ is fluid density, A_j is the projected surface area in direction j, u_1 is the mainstream velocity in the longitudinal direction (x), and $||u||$ is the speed. Note that in this traditional formulation, both the area $A_j(\alpha, \delta, \gamma)$ and the force coefficient $C_j(\alpha, \delta, \gamma, Re)$ are functions of the Euler angles α, δ, and γ, with the latter also depending on the Reynolds number Re. While the projected area A_j has simple geometrical dependence on the Euler angles, the force coefficients have complicated empirical dependence on the orientation (e.g. Ahmad 2005 [9]). Here, we seek an alternative to force coefficients that are empirical functions of Euler angles by considering a formulation where the force coefficients in a frame of reference tied to the object are assumed to be constants, independent of the orientation of the object with respect to the flow. We define the object frame of reference using the following rotation matrix for each extrinsic orientation of our Limpet shell:

$$R_z = \begin{bmatrix} \cos(\alpha) & \sin(\alpha) & 0 \\ -\sin(\alpha) & \cos(\alpha) & 0 \\ 0 & 0 & 1 \end{bmatrix}$$

$$R_y = \begin{bmatrix} \cos(\delta) & 0 & \sin(\delta) \\ 0 & 1 & 0 \\ -\sin(\delta) & 0 & \cos(\delta) \end{bmatrix}$$

$$R_x = \begin{bmatrix} 1 & 0 & 0 \\ 0 & \cos(\gamma) & -\sin(\gamma) \\ 0 & \sin(\gamma) & \cos(\gamma) \end{bmatrix}$$

Then, we have a unique rotation matrix R for each orientation of our shells:

$$R = R_z \cdot R_y \cdot R_x. \tag{6}$$

Our convention for the object frame of reference is such that the longitudinal direction spans from the anterior to the posterior of the shell, and the normal direction spans from the bottom of the shell and upwards. The lateral direction then forms a right handed system along with the longitudinal and the normal directions. When the shell longitudinal and normal directions are initially in the x and y directions of the computational frame, and the shell is subsequently rotated by the Euler angles α, δ, and γ, the rotation matrix defined above can be used to transform vectors to the object frame. A visualization of this convention is shown in Fig. 1.

For example, we use this rotation matrix to convert our simulated forces and velocity components from the computational frame of reference to the object frame of reference:

$$\hat{F}_i = R_{ij} F_j \tag{7}$$

and

$$\hat{U}_j = R_{j1} u_1, \tag{8}$$

where $i = 1$ for the longitudinal components and $i = 2$ for the normal components in the object frame. Then, we hypothesize that the forces in the object frame of reference are related linearly to the respective velocity components as follows:

$$\hat{F}_i = \frac{1}{2} \hat{U}_j \rho A_{ref} C_{ij} ||u||, \tag{9}$$

where the tensor coefficients C_{ij} are assumed to be orientation-independent and A_{ref} is a constant reference area of the considered object. Here, and in all that follows, "^" will denote variables in the object frame of reference. Note, that $\hat{F}$ still depends on orientation via $\hat{U}$. Once we have evaluated the coefficients C_{ij} in the object frame, we transform the forces back to the computational frame of reference using the rotation matrix:

$$F_j = R^T_{ij}(\alpha, \delta, \gamma) \hat{F}_i(\alpha, \delta, \gamma). \tag{10}$$

2.2 Numerical simulations

We use the shear stress transport (SST) $k - \omega$ turbulence model with boundary layer resolving grids in our RANS simulations to obtain our fluid drag and lift forces, as suggested by Ahmad [9]. The SST $k - \omega$ model is a commonly used turbulence model in the family of RANS turbulence models, which models all effects of turbulence. The standard $k - \omega$ turbulence model is designed for low Reynolds numbers, as

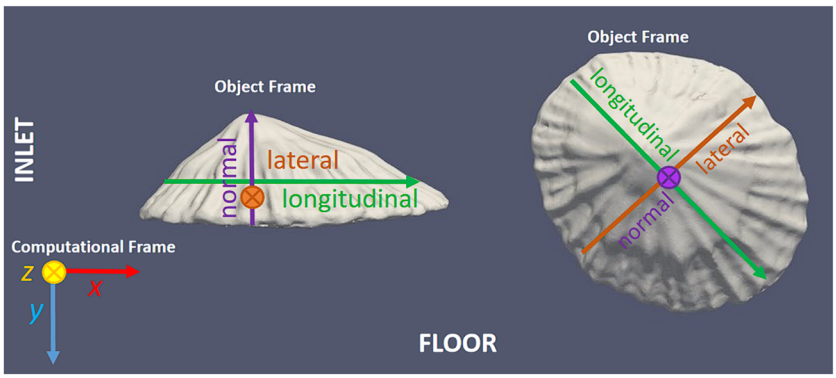

(a)

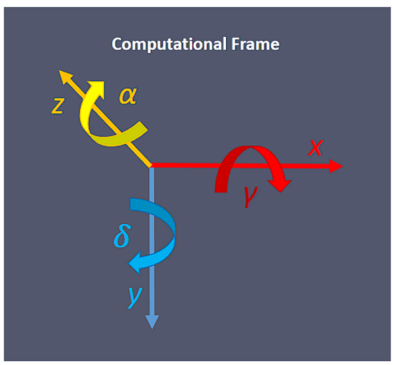

(b)

Fig. 1 Conventions for the computational and object frames of reference

Table 1 Boundary conditions for simulations

Parameter	Floor	Top & Side	Geometry	Inlet
U	`noSlip`	`slip`	`fixedVal (0 0 0)`	`fixedProfile`
k	`fixedVal 0`	`slip`	`fixedVal 0`	`fixedVal I.C.`
ω	`fixedVal` ∞	`slip`	`fixedVal` ∞	`fixedVal I.C.`
ν_t	`fixedVal 0`	`calculated`	`fixedVal 0`	`calculated`
p	`zeroGrad`	`slip`	`zeroGrad`	`zeroGrad`

it works best for flow where the boundary layer is relatively thick, allowing the viscous sublayer to be easily resolved [6]. Thus, it is best used for near-wall treatment in simulations. The SST $k-\omega$ model, however, uses model behavior from the $k-\varepsilon$ turbulence model in the free-stream, avoiding sensitivity at the inlet usually found in the standard $k-\omega$ model. The $k-\varepsilon$ model is most reliable for free-shear flows, where the flow develops a mean velocity gradient in the absence of boundaries, so this model would not have worked well for us by itself. The SST $k-\omega$ model uses blending functions F_1 and F_2 to switch from regular $k-\omega$ behavior to $k-\epsilon$ behavior in the free-stream and a limiter of the turbulent kinetic energy production to alleviate spurious energy production in stagnation regions. The main output of the turbulence model is the kinematic eddy viscosity ν_T which provides a closure for the Reynolds stresses in the RANS equations. We use the following values for the constants in the SST $k-\omega$ model: $\beta = 0.075$ in the ω dissipation term, $\beta^* = 0.090$ in the k dissipation term, $\sigma_\omega = 0.500$ in the ω diffusion term, and $\sigma_{\omega 2} = 0.856$ in the k diffusion term.

The RANS simulations are forced using a smooth-wall logarithmic velocity profile at the inlet

$$u(y) = 2.5u_* \ln\left(9y\frac{u_*}{\nu}\right), \tag{11}$$

where u_* is the bottom shear stress velocity. To specify the profile, we estimate u_* from measurements of a reference velocity U at some known height $y = Y$ by solving the following implicit equation

$$U = 2.5u_* \ln\left(9Y\frac{u_*}{\nu}\right) \tag{12}$$

using a combination of the secant method and bisection. The rest of the boundary conditions for our RANS simulations are provided in Table 1. To initialize the $k-\omega$ equations, we use the estimates

$$k = \frac{3}{2}(UI)^2 \tag{13}$$

and

$$\omega = \frac{k^{0.5}}{0.55T}. \tag{14}$$

I is a turbulence intensity dimensionless coefficient, and T is a turbulence length scale.

Wall functions are empirically derived for the purpose of satisfying the physics in the near-wall regions. While they are commonly used, they can sometimes skew results at these near-wall regions, especially for complex flows. Therefore, resolving the boundary layers within the mesh instead is the more accurate route [8]. To resolve the boundary layers in our simulations and avoid the use of wall functions, we will use grid step Δx in near-wall regions with size

$$\Delta x = \frac{\nu}{u_*}, \tag{15}$$

In our OpenFOAM implementation, we chose a bounded, linear Gaussian upwind scheme to discretize the divergence operator, and a linear Gaussian scheme for the gradient operator. Here, Gaussian implies the utilization of Gaussian finite volume integration in the discretization of the divergence aspects. Additionally, we are solving for steady state turbulent flow and therefore use a steady-state time scheme which sets the time derivatives in the simulations to zero; as a result our force predictions would not account for history-dependent effects.

3 Results

3.1 Validation for flat plate at varying angles of attack

To validate the SST $k-\omega$ turbulence model in our RANS simulations, we considered experimental measurements of the drag and lift forces acting on flat plates conducted by Ortiz

Table 2 Initial Conditions (I.C.) for plate simulations

Parameter	Computed value
Reference velocity U	18.9 m/s
Turbulence length scale T	0.24
Intensity I	4.7%
Turbulence kinetic energy k	1.0 m^2/s^2
Turb. specific dissipation rate ω	7.7 s^{-1}

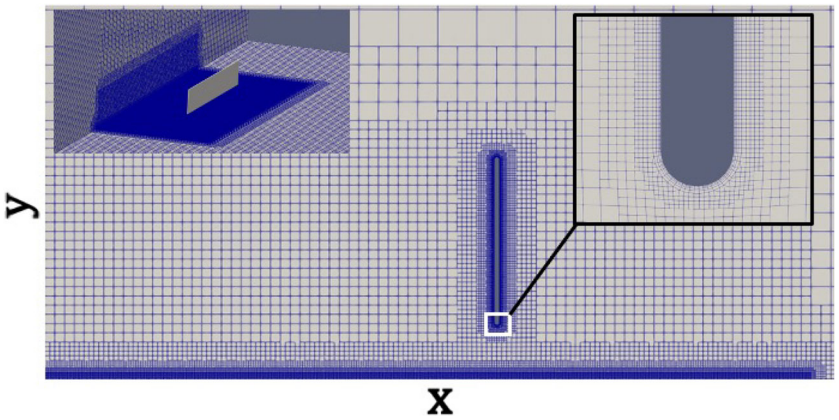

Fig. 2 Cross-section of our 90° plate mesh demonstrating the surface layers and refinement levels of the mesh. Computational domain is 1.20 meters long in the x direction, 0.60 meters tall in the y direction, and 1.60 meters wide in the z direction. Coarsest grid size shown here (refinement level 2) is 0.0167 meters. Plate is sitting 0.15 meters from inlet wall

et al. [7]. We created a stereolithography file of a generic plate that is 0.4 meters wide, 0.066 meters tall, and 0.002 meters thick, identical to Ortiz's plate with an aspect ratio of 6. We chose a computational domain size of 1.20 meters long in the x direction, 0.60 meters tall in the y direction, and 1.60 meters wide in the z direction, and we placed the plates 0.15 meters away from the inlet. A smooth-wall logarithmic velocity profile was specified at the inlet matching the reference velocity $U = 18.9$ m/s at the top of the wind tunnel. The corresponding bottom shear stress velocity $u_* = 0.54m/s$ provided the required boundary layer grid size $\Delta x = 3 \times 10^{-5}m$ from Eq. 15, and Table 2 shows the turbulence parameters defining the initial conditions for k and ω. We then ran RANS simulations with 9 different angles of attack using the SST $k-\omega$ turbulence model and compared our calculated drag and lift coefficient results with those reported in Ortiz et al.

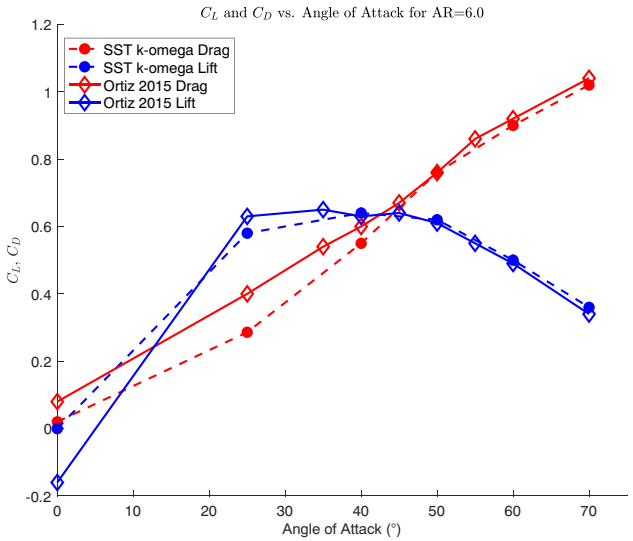

Fig. 3 Simulated (dashed) and experimental (solid) force coefficients for plate with different angle of attack using SST k-ω. All coefficients were computed using $A_{ref} = 0.026\ m^2$

Figure 2 shows a cross-section of the xy-plane of the plate and its position in our simulation domain. Seven refinement levels were used around the plate's surface and four layers with an expansion ratio of $\sqrt{2}$ resulted in a refinement factor of $2^9 = 512$ that reduced the coarse outer mesh grid size of $0.015m$ to the desired surface $\Delta x = 3 \times 10^{-5}m$. Similar refinement was applied at the floor.

We ran our simulations for 3 seconds, allowing for convergence of the drag and lift coefficients, and the results at the end of the simulations are reported in Fig. 3. As in Ortiz et al., the drag and lift coefficients are based on the top surface area of the plate $A_{ref} = 0.066 \times 0.4 = 0.026\ m^2$ (Eq. 9). A comparison of the simulated (dashed lines) and experimental (solid lines) drag and lift coefficients as a function of the pitch angle are shown in Fig. 3. The figure shows a good agreement with a correlation coefficient of 0.95 which confirms that our settings, meshes, and the chosen turbulence model are providing accurate force results.

3.2 Validation for limpet shell at varying reynolds numbers

Having validated that the SST $k-\omega$ turbulence model can reproduce experimental forces on plates, we next simulate the flow around a Limpet shell at various Reynolds number to compare with with the laboratory experiments of Denny (1989) [10] for shells on the bottom with the convex side up. We obtained a stereolithography file of a Limpet Patella shell created by Emily Hauf of the Paleontological Research Institution [18] and scaled the shell to be 8 centimeters long, 2.5 centimeters tall, and 6.8 centimeters wide. These dimensions are 2-3 times larger than the shells considered in Denny which allowed us to achieve the same Reynolds numbers at correspondingly smaller mainstream velocities. For the comparison, we considered shell Reynolds numbers based on the shell length of 24,000, 36,000, 48,000 and 64,000, corresponding to reference flow velocities of

$0.30\ m/s, 0.45\ m/s, 0.60\ m/s$ and $0.80\ m/s$ at the mid-shell elevation $y = 0.012m$ above the bottom.

We chose a computational domain size of 0.72 meters long in the x direction, 0.40 meters tall in the y direction, and 0.56 meters wide in the z direction, and we placed the shells 0.15 meters away from the inlet. The flow is again forced with a smooth-wall logarithmic profile at the inlet that attains the reference velocity at $y = 0.012m$. For the highest Reynolds number $Re = 64,000$, the corresponding bottom shear stress velocity $u_* = 0.038\ m/s$ suggests a minimum grid size $\Delta x = 2.6 \times 10^{-5}\ m$, which is used to set the thickness of mesh layers around the Limpet shell geometry. The same reference velocity suggests $0.0018\ m^2/s^2$ and $0.49\ s^{-1}$, respectively, for the initial turbulence kinetic energy k and turbulence specific dissipation rate ω. We used the same boundary conditions stated in Table 1. Figure 4 shows the surface mesh of our Limpet shell where the cells have been set to the desired Δx, and Fig. 5 shows a cross-section of the xy-plane of our initially oriented shell. Here, one can note the two surface layers and six refinement levels surrounding the surface mesh of our shell.

We again report the results at the end of the simulated 3 second period and compare our simulated drag (Fig. 6, red symbols)to the experimental values for the limpet shell considered in Figure 3b of Denny 1989. For this comparison, the drag coefficient is defined using the cross-section area of the shell projected in the upstream direction. In Fig. 6, circles represent the baseline shell orientation of concave side down and anterior-facing upstream, while triangles correspond to orientation with shell side-facing upstream and concave side down.

We notice a good match between our simulated drag coefficients and Denny's experimental drag coefficients except at the lowest Reynolds number. In this regard, we note that while the standard $k-\omega$ turbulence model is designed for low Reynolds numbers, the SST $k-\omega$ model sacrifices some accuracy in low Reynolds number flow in exchange for less sensitivity to the inlet free-stream turbulence properties. Therefore, we believe the drag coefficient underestimations for $\log(Re) = 4.4$ to be due to deficiencies in the turbulence model for low Reynolds numbers.

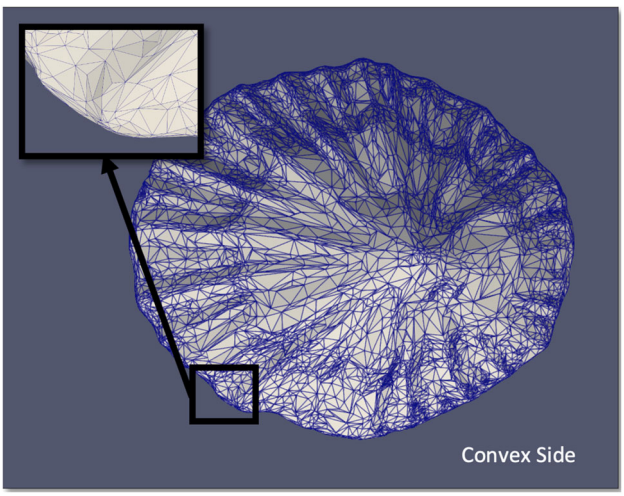

Fig. 4 Surface mesh of the Limpet shell

3.3 Limpet shell in a flow at varying pitch and yaw

We next simulate the flow around a Limpet shell at various orientations in three dimensions to evaluate the respective lift and drag forces. For orientations, we rotated the shell around the $z-$axis and $y-$axis at degrees of 0, 15, 30, 45, 75, 90, 135, 150, and 180. In order to investigate the effect of angle of attack on our shell in the computational frame of reference, Figs. 7 and 8 report the drag and lift coefficients as a function of pitch α (oriented around the $z-$axis) and yaw δ (oriented around the $y-$axis) in degrees, respectively. These coefficients were computed using the total surface area (both concave and convex side) of the Limpet shell $A_{ref} = 0.0105m^2$.

We notice nearly parabolic trends for the drag coefficients, which was expected from Ortiz et al.'s experimental results shown in Fig. 3. We also notice an upward trend of the drag coefficients up to the 90° orientations, and then a downward trend as the shell is then oriented past 90°. The strong symmetry in the drag coefficient trends is expected considering that there is not much of a geometrical difference between the two different lateral sides of our shell. We also note that the trend for the drag coefficients in Figs. 7, 8, and 3 are consistent with Sun et al.'s Eq. 4.

4 Discussion

4.1 Parameterizing the fluid forces on a flat plate

We first implemented our proposed force parameterization using the force and velocity data from the plate experiments of Ortiz et al.. The unique rotation matrices R from Eq. 6 were used to convert the experimental forces and velocities from the laboratory frame of reference to the object frame of reference, and then we performed regressions to estimate the tensor coefficients in Eq. 9. The coefficient matrix resulting from the regressions is

$$C_{ij} = \begin{bmatrix} 0.0567 & 0.0278 \\ -0.1233 & 1.2112 \end{bmatrix} \tag{16}$$

where A_{ref} in Eq. 9 was the top surface area of the plate. We obtain coefficients of determination between reported forces

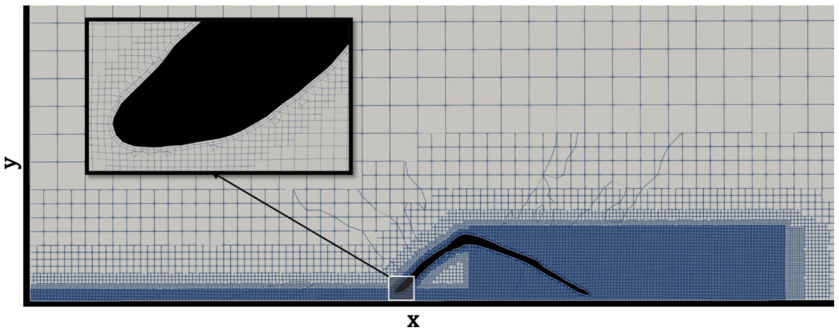

Fig. 5 Cross-section of the Limpet shell mesh demonstrating the surface layers and refinement levels of the mesh. Domain is 0.72 meters long in the x direction, 0.40 meters tall in the y direction, and 0.56 meters wide in the z direction. Coarsest grid size shown here (refinement level 1) is 0.0115 meters. Shell is sitting 0.15 meters from inlet wall

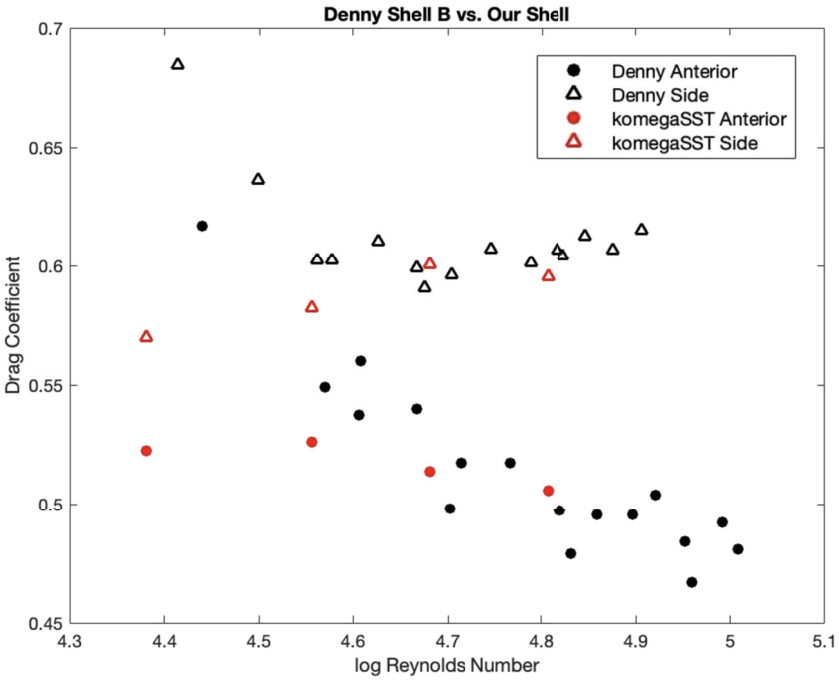

Fig. 6 Simulated drag coefficients for the Limpet shell at four Reynolds numbers and two orientations (red symbols), anterior or lateral side facing upstream, estimated using the respective projected areas, $A_j = 0.0011\ m^2$ and $0.0012\ m^2$. Also shown are the respective drag coefficients of the Limpet Shell in Figure 3b of Denny [10] (black symbols)

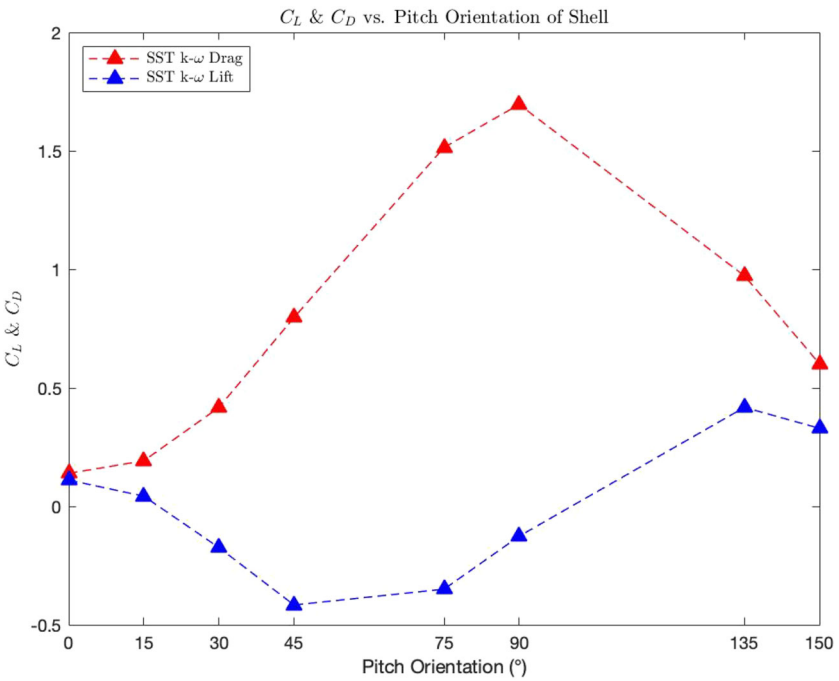

Fig. 7 SST $k-\omega$ drag and lift coefficients as a function of pitch, α, where $A_{ref} = 0.0105m^2$ is the total surface area. Note, that Ortiz considered a $y-$axis that pointed downward rather than upward as we did, resulting in negative lift coefficients in our simulations for pitch angles less than 90°

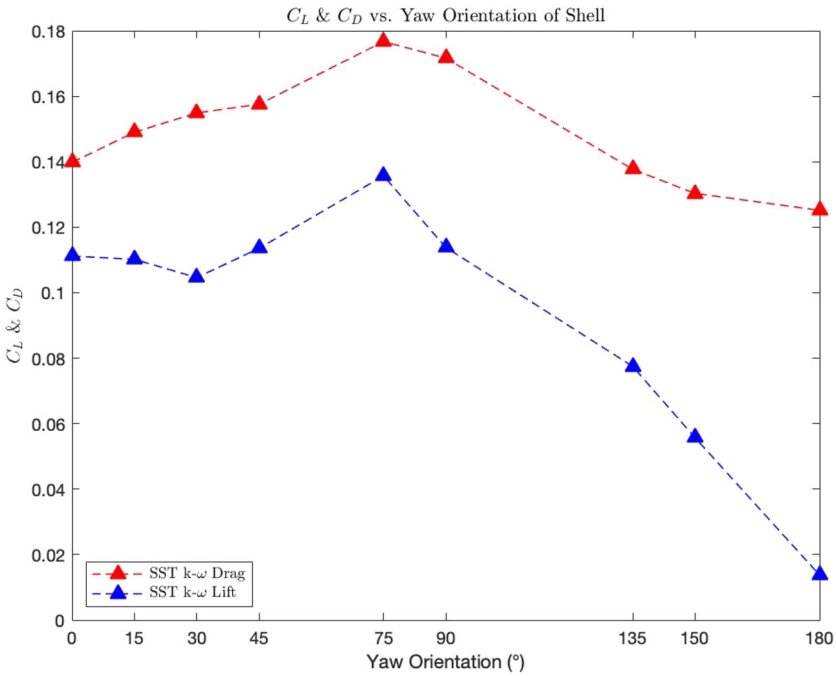

Fig. 8 SST $k-\omega$ drag and lift coefficients as a function of yaw, δ, where $A_{ref} = 0.0105m^2$ is the total surface area

versus predicted forces of 0.91 for the longitudinal forces and 0.76 for the normal forces.

We examine the forces reported by Ortiz et al. versus our predicted results from the regressions for Ortiz's experimental data in Fig. 9. In this figure, the vertical axes are the aerodynamic forces in the object frame of reference, while the horizontal axes are the respective velocity components in the object frame of reference. As the current experiment only considers rotations around the $z-$axis, or α, we only consider the longitudinal, $\hat{U}_1$, and normal, $\hat{U}_2$, velocity components in the figures. In Fig. 9, circles represent the simulated or reported forces, x's represent the predicted forces from our regressions, green and blue represent the longitudinal forces, and red and black represent the normal forces. The figure shows that our parameterization for the forces agrees very well with the forces obtained with the simulations.

We can now obtain an equation for the aerodynamic forces back in the computational frame of reference as a function of

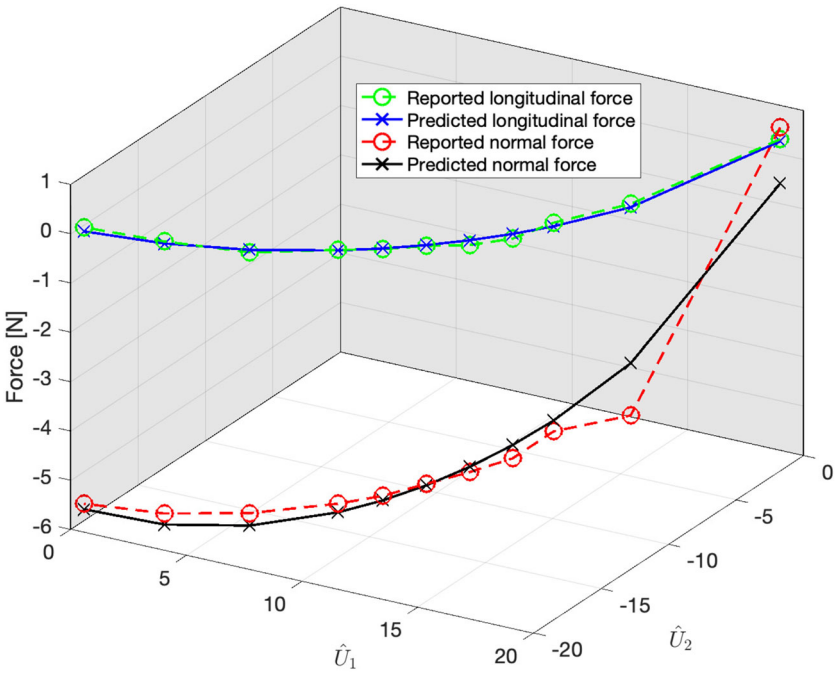

Fig. 9 Simulated and reported aerodynamic forces versus the predicted forces resulting from our force parameterization, specifically for Ortiz's 2-dimensional case of a plate with aspect ratio of 6. The reference area considered here is the top surface area of the plate $A_{ref} = 0.026m^2$

orientations. Because we do not consider various δ and γ for this case of a pitching plate, we only consider α in this final model. Along with the predicted force coefficients in Eq. 16, we substitute

$$\begin{aligned}\hat{U}_j =& R_{j1}u_1 \\ =& \begin{bmatrix}\cos\alpha \\ -\sin\alpha\end{bmatrix} u_1\end{aligned} \tag{17}$$

into the force model described in Eq. 9 to solve for the forces in the object frame of reference:

$$\begin{aligned}\hat{F}_i =& \frac{1}{2}\rho A_{ref}\|u\|C_{ij}\hat{U}_j \\ =& \frac{1}{2}\rho A_{ref}\|u\|u_1 \begin{bmatrix}0.0567\cos\alpha - 0.0278\sin\alpha \\ -0.1233\cos\alpha - 1.2112\sin\alpha\end{bmatrix}\end{aligned} \tag{18}$$

where A_{ref} here refers to the top surface area of the plate.

We can rewrite Jones et al.'s Eqs. 1 and 2 into a concatenated form of the forces and compare the result with our Eq. 18:

$$\begin{bmatrix}X \\ Z\end{bmatrix} = \frac{1}{2}\rho A_{ref}\|u\|^2 \begin{bmatrix}-c_d\cos\alpha + c_l\sin\alpha \\ -c_l\cos\alpha - c_d\sin\alpha\end{bmatrix}.$$

Because our mainstream velocity in Eq. 18 is moving in the longitudinal direction, $u_1 = \|u\|$. Jones et al. considered angles of attack α in which the object is pitching towards the inlet of flow, or negative α's in our frame of reference. Hence, the longitudinal components X of these force equations would have opposite signs. Therefore, we note a strong agreement with Jones et al.'s Eqs. 1 and 2 and our forces in Eq. 18.

Next, we substitute Eq. 18 into our model described in Eq. 10:

$$\begin{aligned}F_j =& R^T_{ji}(\alpha,\delta,\gamma)\hat{F}_i(\alpha,\delta,\gamma) \\ =& \frac{1}{2}\rho A_{ref}\|u\|u_1 \cdot \\ & \begin{bmatrix}0.0567\cos^2\alpha + 0.0955\sin\alpha\cos\alpha + 1.2112\sin^2\alpha \\ -0.1233\cos^2\alpha - 1.1545\sin\alpha\cos\alpha - 0.0278\sin^2\alpha\end{bmatrix}.\end{aligned} \tag{19}$$

Equation (19) provides an explicit model for the aerodynamic forces acting on a flat plate as a function of angle of attack, α.

As stated in Eq. 3, the ratio of the longitudinal and normal force coefficients should result in the tangent of α. We can see that in Eq. 19, our most influential coefficients are 1.2112 for longitudinal force and -1.1545 for normal force, which correspond to the following ratio:

$$\frac{1.2112\sin^2\alpha}{-1.1545\sin\alpha\cos\alpha} \approx \tan\alpha. \tag{20}$$

As $\alpha \to 0$, the coefficients mentioned above lose their influence, and Eqs. 3 and 20 become invalid. Hence, our force model in Eq. 19 agrees with Ortiz et al.'s theory as long as $\alpha \neq 0$. We also note that Hoerner's prediction, $\sin^2\alpha\cos\alpha$, for the ratio of drag and lift coefficients of ellipsoid and fiber-shaped particles is not consistent with our results and those of Ortiz et al. for rectangular plates [4]. Regarding Sun et al.'s Eq. 4 for the drag coefficient with respect to Ortiz et al.'s data, we notice that the simulated and reported drag coefficients in Fig. 3 follow a sine function, consistent with the formula suggested by Sun et al.

4.2 Parameterizing the fluid forces on a Limpet Shell

For the 3-dimensional case of the Limpet shell, we consider a Reynolds number of 12,000 and 67 unique orientations where all 3 axes are rotated. We follow the same procedure described in the previous section to evaluate the forces in the object frame of reference with Eq. 9, and then we solve for the predictive force model in the computational frame of reference with Eq. 10. We perform regressions to solve for the predicted force coefficients C_{ij}, but because we are considering 3-dimensional data, the predicted force coefficients C_{ij} will now result in a 3×3 matrix where $i = 1$ stands for longitudinal forces, $i = 2$ for normal forces, and $i = 3$ for lateral forces. For the columns, $j = 1$ for the force coefficients resulting from the longitudinal component of flow in the object frame, $\hat{U}_1$, $j = 2$ for the force coefficients resulting from the normal flow component in the object frame, $\hat{U}_2$, and $j = 3$ for the force coefficients resulting from the lateral flow component in the object frame, $\hat{U}_3$. The 3-dimensional coefficient matrix resulting from the regressions is

$$C_{ij} = \begin{bmatrix}0.4804 & -0.0376 & 0.0216 \\ 0.1082 & 1.2722 & -0.0962 \\ 0.0026 & 0.2045 & 0.7868\end{bmatrix} \tag{21}$$

Here, $A_{ref} = 0.0105m^2$ from Eq. 9 is again the total surface area of the shell. The regression fit of the computed and predicted forces in the object frame is characterized with

coefficients of determination 0.80 for the normal forces and 0.51 for the longitudinal forces. The low value of the coefficient of determination for the longitudinal forces is due to a handful of outliers that will be examined in more details below.

In Figs. 10 and 11, we show the computed longitudinal and normal hydrodynamic forces versus the predicted hydrodynamic forces, respectively. We consider a 2-dimensional projection of the 3-dimensional regressions for visualization purposes. We use colored lines and x's to represent the plane of best-fit of the simulated forces, or our predicted forces, where different colors correspond to their respective unique values of the lateral velocity component in the object frame. We use black circles to represent the computed forces from the simulations. The vertical axes are the hydrodynamic forces in the object frame of reference, while the horizontal axes are the respective longitudinal and normal velocity components in the object frame of reference.

Similar to the previous section, we would now like to express an equation for the hydrodynamic forces back in the computational frame of reference as a function of orientations. In this case of 3-dimensional data, we will be considering α, δ, and γ in this final model. Along with the predicted force coefficients in Eq. 21, we substitute

$$\begin{aligned}\hat{U}_j =& R_{j1}u_1 \\ =& \begin{bmatrix} \cos\alpha\cos\delta \\ -\sin\alpha\cos\delta \\ -\sin\delta \end{bmatrix} u_1 \end{aligned} \tag{22}$$

into the force model described in Eq. 9 to solve for the forces in the object frame of reference:

$$\begin{aligned}\hat{F} =& \frac{1}{2}\rho A_{ref}\|u\|C_{ij}\hat{U}_j \\ =& \frac{1}{2}\rho A_{ref}\|u\|u_1 \cdot \\ & \begin{bmatrix} 0.4804\cos\alpha\cos\delta + 0.0376\sin\alpha\cos\delta - 0.0216\sin\delta \\ 0.1082\cos\alpha\cos\delta - 1.2722\sin\alpha\cos\delta + 0.0962\sin\delta \\ 0.0026\cos\alpha\cos\delta - 0.2045\sin\alpha\cos\delta - 0.7868\sin\delta \end{bmatrix} \end{aligned} \tag{23}$$

where A_{ref} is the total surface area of the shell.

Next, we substitute Eq. 23 into our model described in Eq. 10 and solve for our model that can be used to predict the hydrodynamic forces:

$$\begin{aligned}F_j =& R^T_{ji}(\alpha,\delta,\gamma)\hat{F}_i(\alpha,\delta,\gamma) \\ =& \frac{1}{2}\rho A_{ref}\|u\|u_1 \cdot \\ & \begin{bmatrix} \cos\alpha\cos\delta & & \\ \cos\alpha\sin\delta\sin\gamma - \sin\alpha\cos\gamma & & \\ \cos\alpha\sin\delta\cos\gamma + \sin\alpha\sin\gamma & & \end{bmatrix} \\ & \begin{bmatrix} \sin\alpha\cos\delta & -\sin(\delta) \\ \sin\alpha\sin\delta\sin\gamma + \cos\alpha\cos\gamma & \cos\delta\sin\gamma \\ \sin\alpha\sin\delta\cos\gamma - \cos\alpha\sin\gamma & \cos\delta\cos\gamma \end{bmatrix} \cdot \\ & \begin{bmatrix} 0.4804\cos\alpha\cos\delta + 0.0376\sin\alpha\cos\delta - 0.0216\sin\delta \\ 0.1082\cos\alpha\cos\delta - 1.2722\sin\alpha\cos\delta + 0.0962\sin\delta \\ 0.0026\cos\alpha\cos\delta - 0.2045\sin\alpha\cos\delta - 0.7868\sin\delta \end{bmatrix} \end{aligned} \tag{24}$$

Similar to Eq. 19, 24 provides an explicit model for predicting the hydrodynamic forces acting on a Limpet shell as an analytical function of the shell orientation angles α, δ, and γ. While both the 2D and 3D coefficients in Eqs. 16 and 21 are diagonally dominant, they differ significantly in C_{11}. We see that for the plate, C_{11} is essentially zero, while the coefficient is significant for the limpet shell. To understand the difference between the C_{11} force coefficients for the limpet shell and the plate, we isolate the longitudinal forces by examining the special case of the forces acting on the limpet shell for α, δ, and $\gamma = 0$:

$$\begin{aligned}F_j =& R^T_{ji}(0,0,0)\hat{F}_i(0,0,0) \\ =& \frac{1}{2}\rho A\|u\|u_1 \begin{bmatrix} 0.4804 \\ 0.1082 \\ 0.0026 \end{bmatrix} \end{aligned} \tag{25}$$

Clearly, the longitudinal and the normal force acting on the limpet are not zero unlike the plate. This is because the limpet has a nonzero projected area even when α, δ, and γ are zero, while the plate has a negligible projected area in this case. We also note that the C_{22} coefficients for the limpet shell and the plate do not differ significantly, and we do not expect to see a significant change in this coefficient if the shell is distorted slightly. We do expect to see a proportional reduction in C_{11} as the shell shape becomes flatter.

In Fig. 12, we investigate the surface pressure distributions on two of the outlier cases with extreme longitudinal force in Fig. 10. As a naming convention for the orientations, we use

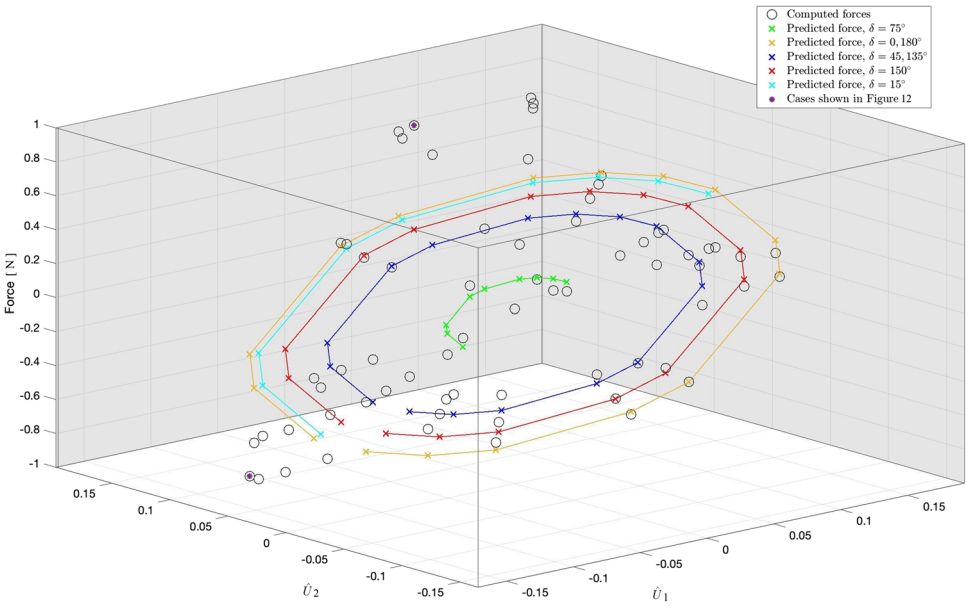

Fig. 10 Longitudinal force regression as a function of $\hat{U}_1$ and $\hat{U}_2$ for different $\hat{U}_3$ values indicated by different colors

$(\alpha\ \delta\ \gamma)°$. Specifically in Fig. 12, we plot the surface pressure of shell orientations (75 30 0)° and (135 0 0)°, where (75 30 0)° represents an orientation with a high, positive longitudinal force and (135 0 0)° represents an orientation with a high, negative longitudinal force. The direction of flow can be interpreted by the red $x-$axis arrow displayed for each case. For orientation (75 30 0)°, we can see a concentration of very high pressure acting on the anterior of the shell contrasted with a slightly lower pressure on the posterior side. This pattern results in a significant longitudinal force despite the fact that the longitudinal flow component is small. For orientation (135 0 0)°, we notice a concentration of high pressure acting on the posterior of the shell and a much lower pressure occurring on the anterior. As expected, this results in a very high, albeit negative, longitudinal force acting on the shell as the direction of flow is travelling in nearly the opposite direction relative to the object frame. As for the normal forces, we notice the trend of high normal forces being given by high $\hat{U}2$ velocity components in Fig. 11. We also note that the cluster of simulated data points near a nearly zero normal force in Fig. 11 all correspond to orientations of the shell being nearly perpendicular to the flow with respect to the object frame. The outliers in Figs. 10 and 11 may require the addition of nonlinear terms and and will be investigated in a separate work focusing on triangular shell fragments.

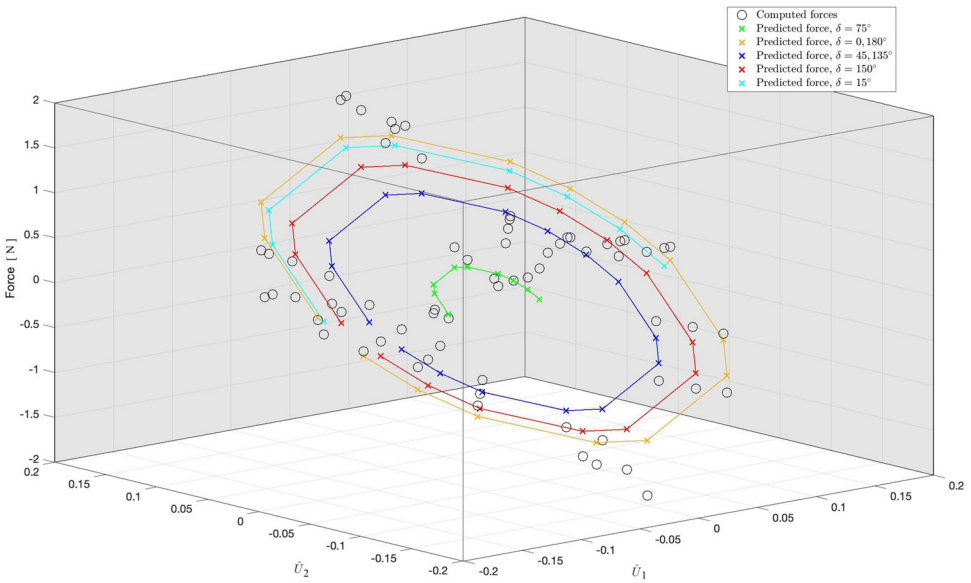

Fig. 11 Normal force regression as a function of $\hat{U}_1$ and $\hat{U}_2$ for different $\hat{U}_3$ values indicated by different colors

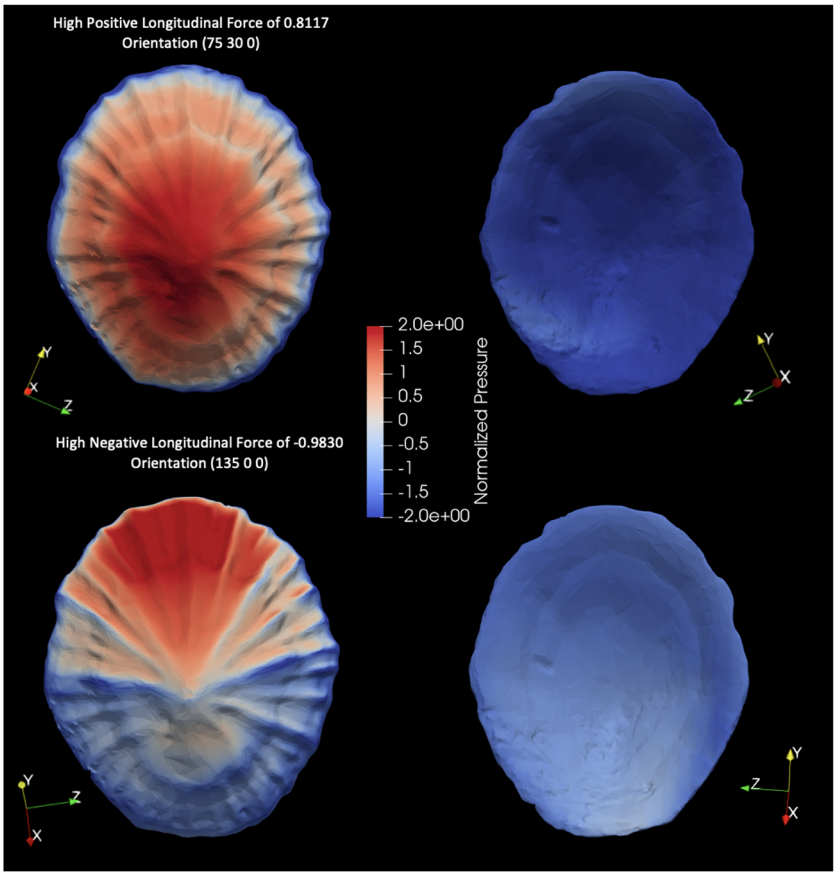

Fig. 12 Comparing surface pressure of (75 30 0)° and (135 0 0)° simulated data points. These points correlate to a high, positive longitudinal force and a high, negative longitudinal force, respectively. Pressure is normalized by ρ and mainstream velocity squared

5 Conclusion

In this paper, we investigated a parameterization of the hydrodynamic forces on a Limpet shell that includes an explicit dependence on the three Euler angles defining the shell orientation with respect to the main flow. The parameterization assumes that the force and the flow vectors in the object frame of reference are linearly related with nine orientation-independent tensor coefficients as defined in Eqs. 9 and 10. We tested the parameterization using RANS simulations to estimate the drag and lift forces on a rectangular plate and a Limpet shell at different orientations.

The accuracy of the SST $k-\omega$ turbulence model used in the RANS simulations was first tested by running various simulations on flat plates with varying angles of attack and then comparing the simulated aerodynamic drag and lift coefficients with those measured in wind tunnel experiments by Ortiz et al. We calculated coefficients of determination of approximately 0.95 for both the drag and lift coefficients, and we concluded that our turbulence model used in our RANS simulations is reporting reliable estimates. For further turbulence model verification, we compared simulated drag and lift coefficients with the ones reported in flow tunnel experiments with Limpet shells by Denny 1989 at the same orientations and found good agreement with the observed dependence of the drag coefficients on the Reynolds number (Fig. 6).

We first tested the force parameterization using the measured forces in the pitching plate experiments of Ortiz et al. where the force and flow vectors in the object frame are 2-dimensional and only four tensor coefficients are needed to define the parameterization. We found that our parameterization fits the measured data with coefficients of determination of 0.76 for normal forces and 0.91 for longitudinal forces (Fig. 9) and noted a strong agreement between the predicted forces in Eq. 18 and Jones et al.'s Eqs. 1 and 2. We also noted a strong agreement between our ratio of the 2-dimensional drag and lift coefficients in Eq. 20 and the ratio introduced by Torres in Ortiz et al. 2015.

We then proceeded to evaluate the parameterization of the forces on a Limpet shell using the force estimates obtained in our RANS simulations. The resulting 3-dimensional parameterization provided by the coefficients in Eq. 23 was found to be effective in predicting the normal forces with a coefficient of determination of 0.80 for the predicted normal forces, but somewhat less effective for the longitudinal forces where the

coefficient of determination was 0.51. The reduced effectiveness of the parameterization for longitudinal forces was found to be limited to a small number of outliers characterized with the highest longitudinal forces and corresponding to a few specific orientations with low values of yaw and roll angles. Improvements of longitudinal force parameterizations with the addition of cubic terms will be investigated in a separate study focusing on triangular spherical shells objects. Considering the overall good performance of the parameterizations, we believe that the proposed new approach of predicting forces on rotating objects would be valuable for modeling the dynamics of shell-shaped objects in Lagrangian particle simulations. The advantage of the new parameterization is that it provides explicit expression for the forces in the computational frame of reference as a function of the Euler angles defining the orientation of the object, e.q. Eq. 24. We conclude by noting that the coefficients obtained here for a Reynolds number of 12,000 can be easily extended to other Reynolds numbers using the measured dependencies in Fig. 6. We are also considering additional RANS simulations for shell fragments where the goal is to obtain parameterizations with an explicit dependence of the tensor coefficients on the shape characteristics such as aspect ratio and curvature.

Acknowledgements Carley Walker and Julian Simeonov were supported through base funding of the U.S. Naval Research Laboratory. This work was supported in part by a grant of computer time from the DoD High Performance Computing Modernization Program. Portion of this work was performed while Ian Adams held an National Research Council Research Associateship award at the U.S. Naval Research Laboratory.

Author Contributions Carley Walker designed and performed the simulations, performed the computations, and analyzed the data. Julian Simeonov conceived and directed the project as well as verified methods and analyses. Ian Adams designed and performed the plate simulations during the revision. All three authors discussed the results and contributed to the final manuscript.

Funding The authors were supported through base funding of the U.S. Naval Research Laboratory.

Availability of data and materials Data can be made available upon request to the corresponding author.

Code Availability Code is open-source and can be made available upon request to the corresponding author.

Declarations

Competing interests The authors have no competing interests to declare that are relevant to the content of this article.

Consent for publication The authors confirm that this manuscript has been read and approved for submission by all named authors.

References

1. Rosendahl, L.: Using a multi-parameter particle shape description to predict the motion of non-spherical particle shapes in swirling flow. Appl. Math. Model. **24**, 11–25 (2000)
2. Mandø, M., Rosendahl, L.: On the motion of irregular particles at high Reynolds number. Powd. Tech. **202**, 1–13 (2010)
3. Pesavento, U., Wang, J.Z.: Falling paper: Navier-Stokes solutions, model of fluid forces, and center of mass elevation. Phys. Rev. Lett. **93**(14)(2004)
4. Hoerner, J.: Fluid Dynamics Drag. Hoerner Fluid Dynamics (1965)
5. Sun, Q., Zhao, G., Peng, W., Jiang, Y., Yu, S.: Numerical predictions of the drag coefficients of irregular particles in an HTGR. Ann. of Nuc. Energy. **115**, 195–208 (2018)
6. Menter, F.R.: Two-equation Eddy-Viscosity turbulence models for engineering applications. AIAA J. **32**, 1598–1605 (1994)
7. Ortiz, X., Rival, D., Wood, D.: Information processing at Forces and moments on flat plates of small aspect ratio with application to PV wind loads and small wind turbine blades. Energies. **8**, 2438–2453 (2015)
8. Eça, L., Saraiva, G., Vaz, G., Abreu, H.: The Pros and Cons of Wall Functions. Proc. of the ASME 2015 34th Int. Conf. on Ocean, Offshore and Arctic Eng. (2015)
9. Ahmad, K.A., McEwan, W., Watterson, J.K. and Cole, J.: RANS turbulence models for pitching airfoil. WIT Trans. on The Built Env. **84** (2005)
10. Denny, M.: A Limpet shell shape that reduces drag: laboratory demonstration of a hydrodynamic mechanism and an exploration of its effectiveness in nature. Can. J. Zoo. **67**, 2098–2106 (1989)
11. Denny, M.: Limits to optimization: fluid dynamics, adhesive strength and the evolution of shape in Limpet shells. J. of Exp. Bio. **203**, 2603–2622 (2000)
12. Joelchorin, A.: Numerical study of slightly viscous flow. Comp. Wind Eng. 1 (1993)

13. Shademan, M., Naghib-Lahouti, A.: Effects of aspect ratio and inclination angle on aerodynamic loads of a flat plate. Adv. in Aero. **2**, 14 (2020)
14. Jones, D.A., Clarke, D.B., Brayshaw, I.B., Barillon, J.L., Anderson, B.: The calculation of hydrodynamic coefficients for underwater vehicles. Def. Sci. and Tech. (2002)
15. Torres, G.E., Mueller, T.J.: Low aspect ratio aerodynamics at low Reynolds numbers. AIAA J. **42**, 865–873 (2004)
16. Dioguardi, F., Mele, D., Dellino, P.: A new one-equation model of fluid drag for irregularly shaped particles valid over a wide range of reynolds number. J. of Geo. Research: Solid Earth **123**, 144–156 (2018)
17. Leith, D.: Drag on nonspherical objects. Aero Sci. and Tech. **6**(2), 153–161 (1987)
18. Bay, J.: Gastropod: Patella sp. (PRI 76781). Sketchfab (2018). https://skfb.ly/6ARwp